Photolysis of water-radical ions H_2O^+ in the xuv: Fragmentation through dicationic states

H. B. Pedersen,[1,*] C. Domesle,[2] L. Lammich,[1] S. Dziarzhytski,[3] N. Guerassimova,[3] R. Treusch,[3] L. S. Harbo,[1] O. Heber,[4] B. Jordon-Thaden,[2] T. Arion,[5] M. Förstel,[5] M. Stier,[5] U. Hergenhahn,[5] and A. Wolf[2]

[1]*Department of Physics and Astronomy, Aarhus University, DK-8000 Aarhus C, Denmark*

[2]*Max-Planck-Institut für Kernphysik, D-69117 Heidelberg, Germany*

[3]*HASYLAB at DESY, Hamburg, Germany*

[4]*Department of Particle Physics, Weizmann Institute of Science, Rehovot 76100, Israel*

[5]*Max-Planck-Institut für Plasmaphysik, EURATOM Association, 85748 Garching, Germany*

(Received 20 November 2012; published 2 January 2013)

The photofragmentation of the water cation H_2O^+ through dicationic states has been studied at 35.0 ± 0.2 nm (35.4 ± 0.3 eV) and 21.8 ± 0.2 nm (56.8 ± 0.5 eV) with a crossed ion-photon beams experiment at the free electron laser FLASH. The dissociation of the dications is found to be similar at the two wavelengths and to proceed into $O^0 + 2H^+$, $OH^+ + H^+$, and $O^+ + H_2^+$, with determined ratios $\sigma_{OH^+ + H^+}/\sigma_{O^+ + H_2^+} = 4.2 \pm 0.3$ and $\sigma_{OH^+ + H^+}/\sigma_{O^0 + 2H^+} > 0.7$. The measured kinetic-energy releases for these processes are consistent with three-body breakup ($O^0 + 2H^+$) occurring mainly through the $2\,^3A''$ and $2\,^1A''$ states of H_2O^{2+} and two-body breakup ($OH^+ + H^+$) occurring through $X\,^3A''$, $1\,^3A'$, and $1\,^1A''$ states of H_2O^{2+}, as predicted in a recent theoretical study [Gervais *et al.*, J. Chem. Phys. **131**, 024302 (2009)]. In addition to the kinetic-energy releases, we also report on fragment correlation in the three-body channel where the two protons carry the major part of the released momentum.

DOI: 10.1103/PhysRevA.87.013402 PACS number(s): 33.80.Gj

I. INTRODUCTION

The water cation H_2O^+ occurs in several natural environments where molecular gas is exposed to ionizing radiation. It has been directly observed in the upper atmosphere [1] and in the tails of several comets [2–7] through its emission spectrum in the visible (vis) range; these observations have been used to indirectly identify the presence of neutral water in comets, since H_2O molecules themselves do not show a vis emission spectrum. Recently, the astrophysical importance of H_2O^+ has been highlighted by several observations of both H_2O^+ and other oxygen hydride ions (OH^+ and H_3O^+) using the Herschel Space Observatory [8–11]. Reactions of oxygen and its smaller hydrides are parts of models of the interstellar chemistry in various environments [12–16], where in particular H_2O^+ ions are formed in reactions between H_2 and OH^+, while being depleted by further reactions with H_2 to form H_3O^+ and by dissociative recombination. The presence of ionizing radiation in such environments will destroy these ions via dicationic (H_2O^{2+}) states leading to energetic atomic (H^+, H^0, O^+, O^0) or molecular (H_2^+, H_2^0, OH^+, OH^0) products. While H_2O^+ and other oxygen hydride ions are included in models of interstellar chemistry [12–16], the fragmentation of water cations has so far not been considered.

In this paper we investigate the fragmentation of isolated H_2O^+ ions under ionizing radiation in the form of monoenergetic photons in the extreme ultraviolet (xuv) regime [35.0 nm (35.4 eV) and 21.8 nm (56.8 eV)] using intense pulses of radiation from a free electron laser [17,18]. By xuv irradiation of these ions, dications (H_2O^{2+}) are formed, presumably with similar nuclear conformations as the monocations (Franck-Condon region) and we study the fragmentation dynamics that reflects the properties of the accessed dicationic potential energy surfaces (PESs).

The water dication (H_2O^{2+}) has previously been experimentally investigated exclusively in studies of double ionization of neutral H_2O with projectiles of ions [19–24], electrons [25–28], and photons [29–39]. Theoretically, the water dications have been the subject of several studies [40–44]. Due to the nature of these types of ionizing radiation, various aspects of the PESs of the water dication have been accessed. In a recent theoretical study, Gervais *et al.* [44] emphasized the fact that (prior to this study) the PESs of the water dication have never been investigated by direct excitations from the water monocation.

Gervais *et al.* [44] performed *ab initio* calculations on eight PESs of H_2O^{2+} corresponding to ionization of various valence electron orbitals. They further investigated the dissociation dynamics in the Franck-Condon regions of both the neutral (H_2O) and the two electronic states ($\tilde{X}\,^2B_1$ and $\tilde{A}\,^2A_1$) of the monocation (H_2O^+) by direct three-body classical dynamics simulations on the PESs. Thus, they obtained spectra of fragment kinetic-energy releases, which, in principle, allows a detailed comparison to experiments that include momentum resolved detection of the emerging photofragments.

Figure 1 shows schematically the electronic transitions and PES energies for the dication as described by Gervais *et al.* [44], as well as the final dissociation limits for the fragmenting dicationic system. The monocation has three low-lying electronic states of different geometry (see, e.g., Ref. [45] for a review) from which dicationic states can be reached by photoabsorption. The ground state ($\tilde{X}\,^2B_1$) is bent with a geometry similar to neutral water, the first excited state ($\tilde{A}\,^2A_1$) is linear, while the second excited state ($\tilde{B}\,^2B_2$) is strongly bent. Gervais *et al.* [44] argued that with respect to ionization from the monocation, five states ($X\,^3A''$, $1\,^1A'$,

*To whom correspondence should be addressed: hbjp@phys.au.dk

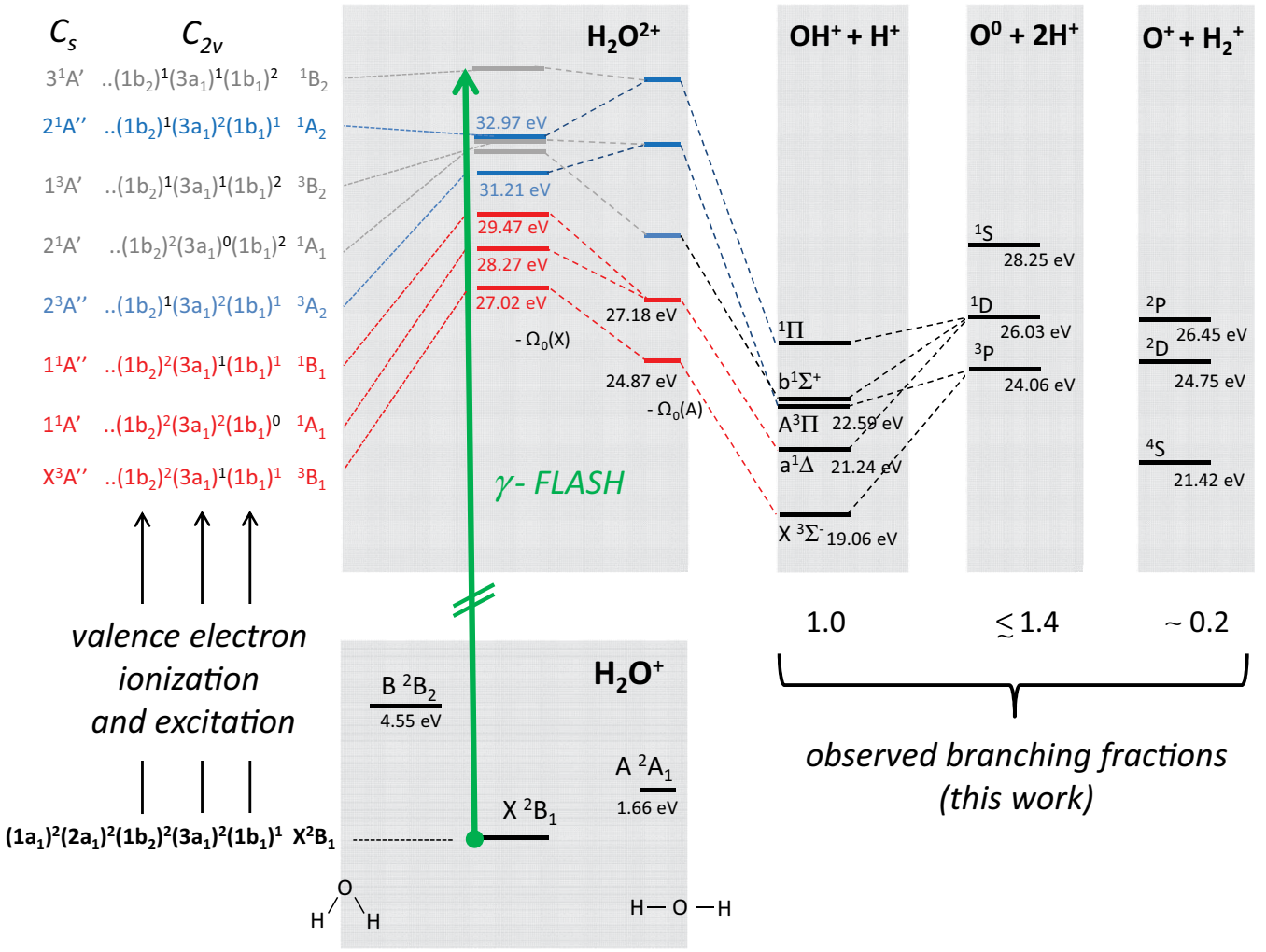

FIG. 1. (Color online) Schematic illustration of the transitions from the water monocation (H_2O^+) to the dissociating dicationic states (H_2O^{2+}) under xuv irradiation based on the calculations by Gervais *et al.* [44]. The electron configurations and vertical ionizations energies are reproduced from Table I of Ref. [44]; in particular, the energetic positions are given as $T_{\tilde{X}}$ and $T_{\tilde{A}}$; that is, the zero-point energies [$\Omega_0(X) = 0.48$ eV for $\tilde{X}\,^2B_1$ and $\Omega_0(A) = 0.50$ eV for $\tilde{A}^2A_1$) have *not* been subtracted. The red-colored levels (X^3A'', $1^1A'$, and $1^1A''$) were predicted to yield two-body fragmentation into $OH^+ + H^+$ and the blue-colored levels ($2^3A''$ and $2^1A''$) to yield three-body fragmentation into $O^0 + 2H^+$ [44]. The gray levels were considered to be unimportant for photoabsorption from the monocation [44].

$1\,^1A''$, $2\,^3A''$, $2\,^1A''$) were most relevant for photoionization since they result from single-electron ionization (levels marked in Fig. 1). The other three states ($2\,^1A'$, $1\,^3A'$, $3\,^1A'$) investigated (marked gray in Fig. 1) resulting from both ionization and excitation were considered important only for double ionization from neutral water. Moreover, upon dissociation starting in the geometry of the ground state of the monocation, the lower two of the relevant states ($X\,^3A''$, $1\,^1A'$), were found theoretically to yield dominantly two-body breakup ($OH^+ + H^+$) while the third state $1^1A''$ yielded both two- and three-body ($O^0 + 2H^+$) fragmentation. The upper two of the relevant states ($2^3A''$ and $2^1A''$) were found to lead exclusively to three-body dissociation. Finally, as a general feature, the two-body channels were found to be associated with significant ro-vibrational excitation of the OH^+ fragment.

With the present study we take a first step towards an experimental investigation of these detailed predictions of the properties of the water dication. The experiment uses a crossed ion-photon beams setup together with intense pulses of xuv light from a free electron laser [17,18] to study the breakup of isolated fast-moving H_2O^+ ions. The applied fragment detection scheme makes it possible to analyze the identity and the momenta of the emerging photofragments.

Consistent with the study of Gervais *et al.* [44], we find that breakup into $O + 2H^+$ and $OH^+ + H^+$ dominates the fragmentation intensity; however, a significant part of the dissociation also leads to $O^+ + H_2^+$. From the measured kinetic-energy releases for the two- and three-body dissociations we also confirm, in general, the predictions made by Gervais *et al.* [44] on the dissociation routes of the dicationic system. As a final aspect, not yet addressed by theory, the measured fragment energies also allow us to analyze the momentum sharing of fragments in the three-body channels. Here we find the dissociation dynamics of the dication to be dominated by a symmetric departure of the two protons that carry most of the released momentum.

II. EXPERIMENT

A. Crossed-beams experiment

The experiment was performed with the ion beam facility TIFF [46] (Trapped Ion Fragmentation with a FEL) which is installed at the Plane Grating Monochromator (PG2) beamline [47] of the Free Electron Laser in Hamburg (FLASH) facility [17,18] at Deutsches Elektronen Synchrotron (DESY).

To produce a fast beam of H_2O^+ we used a hollow cathode ion source located on a high-voltage platform and operated with a gas inlet of pure water vapor with an approximate pressure of 0.1 mbar and sustaining a discharge of 590 V and 24 mA. By extraction to ground potential, a collimated beam of ions with kinetic energy $E_0 = 4.2$ kV was generated. The monoenergetic ion beam was then passed through a magnetic field for mass analysis resulting in a beam of H_2O^+ of $\sim$20 nA.

The mass selected ion beam was electrically guided and collimated by apertures and slits before entering the crossed-beam interaction zone as an essentially parallel beam. During the measurement, the ion beam was chopped [46] into trains of 50 pulses with a width of 1.5 μs matching the time structure of the photon beam from FLASH. After the interaction region the ion pulses were electrically bent into a dump.

The FLASH facility delivered intense horizontally polarized radiation at wavelength 35.0 ± 0.2 nm and 21.8 ± 0.2 nm with a repetition rate of 10 Hz in the form of trains of 50 short (<250 fs) pulses with an average energy of 41 μJ/pulse (at 35.0 nm) and 34 μJ/pulse (at 21.7 nm). The photon pulses were guided through the PG2 beamline with the monochromator operated in zeroth order, resulting in an overall transmission of $T_{PG2} = 0.5 \pm 0.1$, to the crossed ion-photon interaction zone located about 1.5 m before the photon beam focus.

Before and after the interaction region the photon beam was carefully guided through slits of 3×3-mm opening, both to ensure alignment and to prevent stray light generated in the PG2 beamline from reaching the particle detectors. About 3 m downstream from the interaction region, the photon pulses were sent onto an Cu plate biased to -800 V from which a precise timing signal, used to determine the arrival time of the photon pulses, was derived. The spatial overlap of the two beams was verified by scanning a 1-mm-wide needle, inserted at 45°, across the interaction region, thereby simultaneously blocking both beams.

To reduce the background from fragmentation of ions in collisions with the residual gas (mainly H_2), the pressure in the interaction region was kept at UHV conditions (5×10^{-10} mbar) during the measurement.

The data acquisition system was alternated at 20 Hz between four different conditions, namely with (1) both ions and photon pulses in the interaction region, (2) only ion pulses, (3) only photon pulses, and (4) neither ion nor photon pulses (dark counts). By combining these measurements, background-free distributions of single-particle (noncoincidence) events from the ion-photon interaction only were obtained.

To identify correlated events, that is, the collection of particles originate from the same fragmenting ion, coincidence analyses were applied to the data obtained under the condition with both ion and photon pulses in the interaction region, which identified hits on the detectors (DET 1–3) originating from the same ion-photon crossing. A precise evaluation of the contribution from random coincidences in these analyses were obtained by performing an identical analysis for uncorrelated ion-photon crossings.

B. Fragment detection

Figure 2 summarizes schematically the experimental setup around the interaction zone and fragmentation detectors at TIFF. The photon and ion beams cross inside a mechanical structure with several electrodes that allows control of the electric field both parallel (left-right in Fig. 2) and perpendicular (up-down in Fig. 2) to the incoming ion beam. In the present experiment, these electrodes were used to control the local electrical potential (V_c) at the interaction zone, and to create an electrostatic barrier [53] after the interaction zone that prevents slow ions (stemming from ionization in the residual gas) to propagate to the particle detectors. The electrode structure can also be used to facilitate extraction of photoelectrons [48] or to trap ions in the interaction zone; however, these options were not exploited in this experiment.

When the local potential at the interaction zone is biased to V_c, the energy of the reacting ions of charge q_I is $E_I = E_0 - q_I V_c$. After leaving the interaction zone the unfragmented ions emerge again with an energy of E_0. However, photofragments generated on the local potential V_c with mass m_F and charge q_F emerge with a laboratory energy (neglecting here the small kinetic-energy release due to the fragmentation) of $E_F^L = (m_F/m_I)(E_I - q_I V_c) + q_F V_c$. This dependence of the laboratory energy on the fragment properties effectively allows the fragments' identities to be determined (see Sec. III A), for instance, by the resulting time of flight of the fragment to a distant detector.

The photofragments emerging from the interaction zone were detected on one of three multichannel plate (MCP) detectors (DET 1–3) as shown in Fig. 2. Light fragments with sufficient transverse momentum release $\Delta p_F^{\perp}$ (here possibly H, H^+, and $H_2{}^+$) impinge on DET 1, heavy neutral fragments (O^0) propagate unperturbed to impact on DET 2, while heavy charged fragments (O^+ and OH^+) are deflected in the electrostatic mirror and strike the surface of DET 3. As mentioned above, the electron detectors (eDET 1–2) [48] were passive in the present experiment.

The analysis system for heavy charged fragments (i.e., the predeflector and the electrostatic mirror, and DET 3) were developed and installed between the reported measurements at 35.0 nm and 21.8 nm, and while DET 1–2 are both position and time sensitive, the installed DET 3 was only time sensitive.

Thus, for a particle impacting on a detector DET i ($i = 1,2,3$), the time of flight t_i relative to the moment of interaction is recorded, and for DET 1–2 also the transverse positions of impact (x_i, y_i) on the detector surface is determined.

C. Momentum analysis

To analyze the fragmentation kinematics the following normalized coordinates are convenient [46,53]:

$$\rho_i = r_i/\tilde{L}_i, \quad \tau_i = t_i/(\tilde{L}_i/v_I), \tag{1}$$

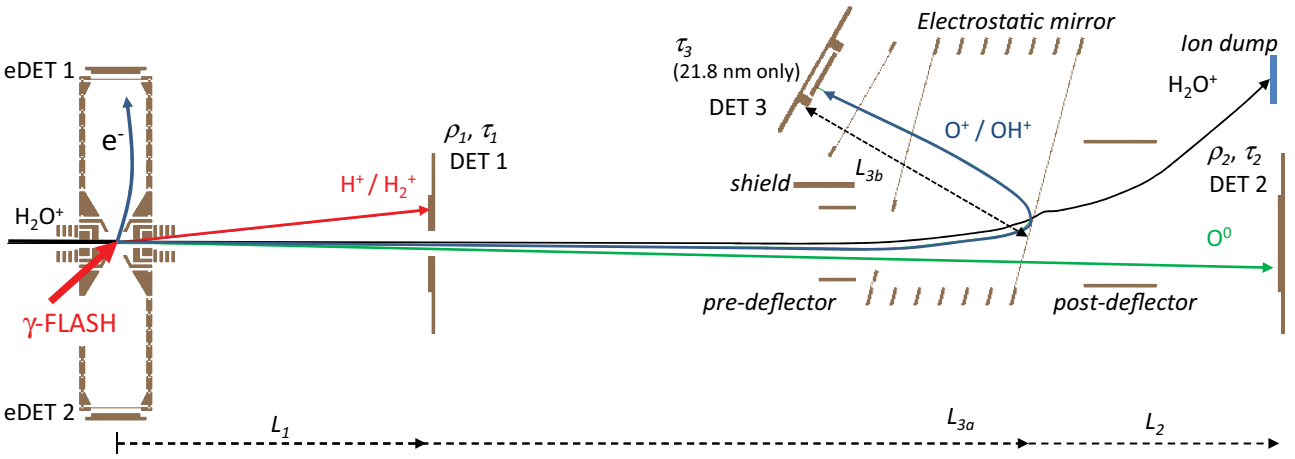

FIG. 2. (Color online) The experimental setup around the interaction region of the TIFF experiment [46] at FLASH [17,18]. For the measurement at 35.0 nm, DET 3, the predeflector and the electrostatic mirror were not installed. The dashed arrows indicate the distances from the interaction point the to DET 1 ($L_1 = 0.273$ m) and to DET 2 ($L_2 = 0.872$ m during measurement at 35.0 nm and $L_2 = 0.967$ m at 21.8 nm), as well as the horizontal distance from the interaction point to the farthest surface of the electrostatic mirror and upwards 150° to the plane defined by the surface of DET 3 ($L_3 = L_{3a} + L_{3b} = 0.975$ m). The solid lines show simulated trajectories for the parent H_2O^+ ion (black line) and some of the heavy photofragments observed in the present experiment. The photoelectron detection capability was not exploited in the this study.

where $r_i = \sqrt{(x_i - x_0)^2 + (y_i - y_0)^2}$ is the transverse distance from the interaction point (x_0, y_0, z_0), $\tilde{L}_i = L_i - z_0$, where L_i is the norminal distance from the interaction point to the detector surface (see Fig. 2), and $v_I = \sqrt{2E_I/m_I}$ is the ion velocity.

The normalized coordinates (ρ_i, τ_i) describe essentially the transverse and longitudinal deflection of the fragment relative to a nondeflected and nonretarded fragment emerging with the beam velocity. When no bias field is applied ($V_c = 0$) or the photofragment is neutral ($q_F = 0$), the gain in transversal ($\Delta p_F^{\perp}$) and longitudinal ($\Delta p_F^{\parallel}$) momentum of a specific fragment due to the photofragmentation reaction can be directly obtained from the normalized coordinates through

$$\Delta p_F^{\parallel}/p_F = (\Delta p_F/p_F)\cos\theta_F = 1/\tau_i - 1 \tag{2}$$

and

$$\Delta p_F^{\perp}/p_F = (\Delta p_F/p_F)\sin\theta_F = \rho_i/\tau_i, \tag{3}$$

where $p_F = m_F v_I$ is the momentum of the undisturbed fragment. The total momentum release Δp_F and fragmentation angle θ_F relative to the laser polarization can now be obtained as

$$\left(\frac{\Delta p_F}{p_F}\right)^2 = \left(\frac{\rho_i}{\tau_i}\right)^2 + \left(\frac{1}{\tau_i} - 1\right)^2 \tag{4}$$

and

$$\tan\theta_F = (\rho_i/\tau_i)/(1/\tau_i - 1). \tag{5}$$

Figures 3(a) and 3(b) show the momentum images obtained from DET 1 and DET 2 at 35.0 nm using Eqs. (2) and (3). As described in the figure caption, Fig. 3(a) also illustrates the detection limitations imposed by the geometrical arrangement of the detectors and by the electrode structure around the interaction region.

To characterize the contributions from three-body dissociation into $O^0 + 2H^+$ or $O^0 + H^+ + H^0$, coincidence analyses between hits on DET 1 and DET 2 were performed. Figure 3(c) shows the resulting (background subtracted) momentum images of particles on DET 1 after requiring coincidence with hits on DET 2. Clearly, the bright circular feature seen in Fig. 3(a), stemming from two-body channels, is no longer present in Fig. 3(c), which holds data for the isolated channels $O^0 + 2H^+$ and $O^0 + H^+ + H^0$. Additionally, it can be recognized from Fig. 3(c) that the single-particle momentum releases in the corresponding three-body channels are for the major part within the detector acceptance limits.

III. RESULTS

A. Fragmentation channels

To gain insight into the mass-to-charge ratio (m_F/q_F) of the observed photofragments we first consider the longitudinal momentum release [Eq. (2)] with and without a local potential (V_c) applied to the interaction zone. It is easily verified [53], for example, from the energy argument given in Sec. II B, that the observed momentum release shifts characteristically for a given fragment identity (m_F/q_F) as a function of the applied potential. Figure 4(a) shows the relative longitudinal momentum release obtained for $V_c = 0$ and for $V_c = 50$ V. The distribution obtained with $V_c = 0$ is centered around zero while the distribution obtained at $V_c = 50$ V is shifted to lower values of $1 - 1/\tau_1$. The leftmost tail of the distribution obtained at $V_c = 50$ V is consistent with a shift corresponding to H^+ fragments, and we identify the major part of the fragments observed on DET 1 to be H^+. However, the width of the observed distribution also allows for H_2^+ fragments to be present. The fact that essentially the full distribution shifts shows that the presence of fragments of neutral hydrogen H^0 is marginal ($\leqslant 5\%$); the distribution of neutral fragments would be centered around zero also with the interaction zone raised to a local potential. Summarizing, the data presented in Fig. 4(a) demonstrate, up to a possible $\leqslant 5\%$ contribution from H^0, that the observed light fragments are mainly H^+ with a possible smaller fraction of H_2^+, thus identifying the fragmentation

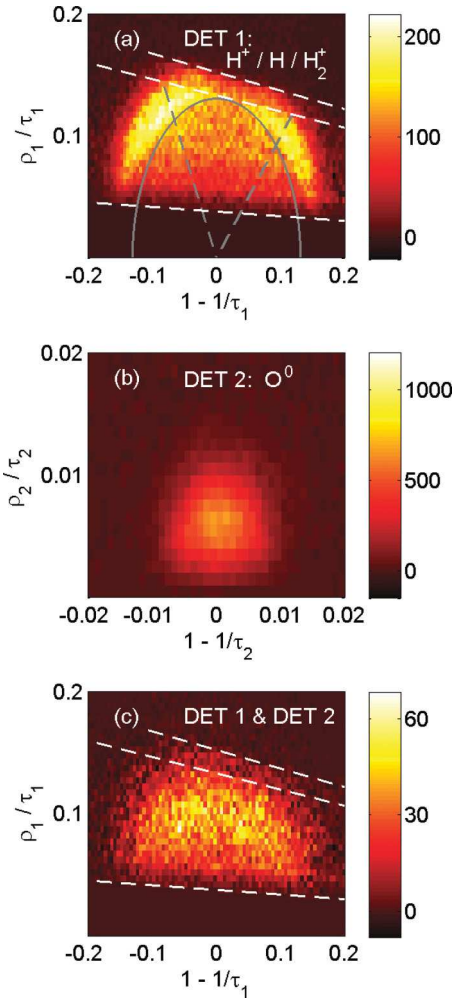

FIG. 3. (Color online) Momentum imaging of photofragments from H_2O^+ under 35.0 nm irradiation using the TIFF experimental system (Fig. 2). (a) Momentum imaging of light fragments with DET 1. White dashed lines mark the limitations imposed by the geometrical arrangement of the experimental system: lower line, effect of the central hole in DET 1 [46]; upper line, effect of the finite size of the detector surface (40-mm outer radius); middle line, limitation from the extended electrode structure close to the interaction region (see Fig. 2). Events observed between the two upper lines result from slightly nonconcentric alignment of the beam in the interaction region. Gray half circle, correlation for two-body breakup with a kinetic-energy release $E_k m_F/(m_I - m_F) = 71.4$ eV ($E_k = 4.2$ eV for $F = H^+$). Dashed gray lines, fragment emission angles $\theta_F = 60^\circ$ (left) and $\theta_F = 135^\circ$ (right) between which fragmentation detection is strongly limited outside the gray circle. (b) Momentum imaging of heavy neutral fragments (here O^0) with DET 2. (c) Momentum imaging of light fragments on DET 1 requiring additionally coincidence with hits on DET 2 (O^0). White dashed lines as in (a).

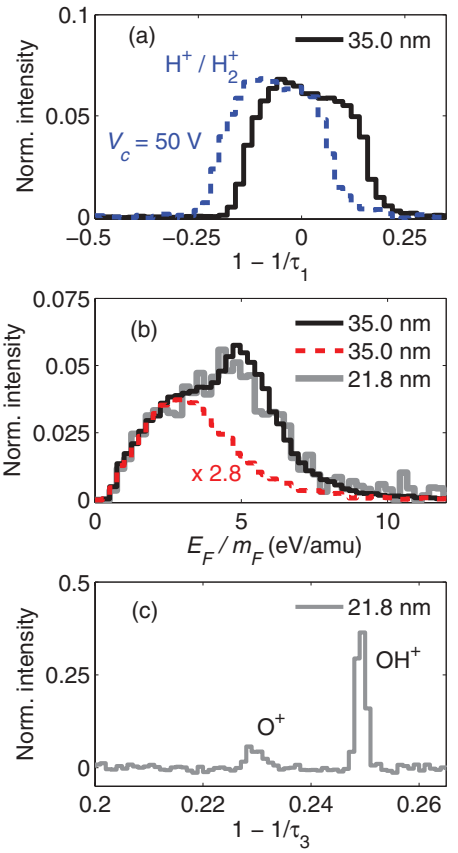

FIG. 4. (Color online) Experimental identification of photofragmentation channels of H_2O^+ under 35.0- and 21.8-nm irradiation using TIFF (Fig. 2). (a) Relative longitudinal momentum [see Eq. (2)] for particles impacting on DET 1 after photoabsorption at 35.0 nm obtained with the interaction zone nonbiased ($V_c = 0$) (solid black line) and biased to $V_c = 50$ V (dashed blue line). Essentially all fragments detected on DET 1 can be identified as charged, that is, H^+ or $H_2{}^+$ (no H^0). (b) Distributions of the ratio of fragment kinetic energy and mass [E_F/m_F; see Eq. (6)] impacting on DET 1 after photofragmentation at 35.0 nm (solid black line) and 21.8 nm (gray line). The dashed red line shows the distributions for the coincidence DET 1 and DET 2, that is, corresponding to the momentum image on Fig. 3(c). (c) Relative longitudinal momentum for particles impacting on DET 3 after photoabsorption at 21.8 nm. The offset of the observed peaks from 0 reflects the deceleration and bending of charged particles in the electrostatic mirror.

channels of xuv irradiated H_2O^+ as $OH^+ + H^+$, $O^0 + 2H^+$, and $O^+ + H_2{}^+$.

To further distinguish between the possible channels, we consider the fragment kinetic energy relative to the mass, obtained as

$$\frac{E_F}{m_F} = \left(\frac{\Delta p_F}{p_F}\right)^2 \frac{E_I}{m_I}, \tag{6}$$

both from all events registered with DET 1 and from those in coincidence with neutral particles impacting on DET 2. The result of this analysis for 35.0-nm irradiation is displayed in Fig. 4(b) as the solid black line (all events) and the dashed red line (events in coincidence with hits on DET 2). The events detected in the coincidence DET 1 and DET 2 can be safely assigned to the channel $O^0 + 2H^+$. Up to a scaling factor related to the total detection efficiency of DET 2, these distributions are very similar at low values of E_F/m_F, but differ significantly for higher values. The difference between the two distributions is identified to originate from the two-body channels $OH^+ + H^+$ and $O^+ + H_2{}^+$ and are further considered below.

The gray curve in Fig. 4(b) shows the distribution of E_F/m_F obtained with the higher photon energy (21.8 nm). Within the experimental uncertainty, the observed distributions at 35.0 and 21.8 nm are identical, demonstrating explicitly that the same ionization-dissociation processes are triggered at these two wavelengths.

With this recognition, the relative significance of the two-body channels $OH^+ + H^+$ and $O^+ + H_2{}^+$ was investigated with the charged-fragment analyzing system (see Fig. 2) installed prior to the measurement at 21.8 nm. Figure 4(c) shows the distribution of the longitudinal momentum release as obtained from DET 3. The two separate peaks can be uniquely identified as O^+ and OH^+, corresponding to different times of flight ($1\text{-}1/\tau_3$) through the electrostatic mirror. Assuming the same detection efficiency of DET 3 for O^+ and OH^+ particles, the ratio of the cross sections leading to the channels $OH^+ + H^+$ and $O^+ + H_2{}^+$ can be obtained from the integral counts of the two peaks in Fig. 4(c),

$$\frac{\sigma_{OH^+ + H^+}}{\sigma_{O^+ + H_2{}^+}} = 4.2 \pm 0.3. \tag{7}$$

Using Fig. 4(b), we can also derive the branching ratio towards the three-body channel. However, a similarly precise statement as in Eq. (7) cannot be made for this value since a considerable part of the intensity of the two-body channels is not detected. Thus, a part of the distribution for $OH^+ + H^+$ is cut by the geometrical detection limits [see Fig. 3(a)], and for $O^+ + H_2{}^+$ a major part of the $H_2{}^+$ fragments pass through the central hole of DET 1 and are not registered. Making the simplifying assumption that all two-body events recorded on DET 1 stem from the largely dominant $OH^+ + H^+$, we obtain a lower limit on the ratio of the two dominating channels,

$$\frac{\sigma_{OH^+ + H^+}}{\sigma_{O^0 + 2H^+}} > 0.7. \tag{8}$$

B. Three-body fragmentation dynamics: $H_2O^{2+} \rightarrow O^0 + 2H^+$

For the photofragmentation events leading to $O^0 + 2H^+$, we detect in coincidence two protons on DET 1 and an oxygen atom on DET 2 (Fig. 2). The recorded time and position information from these detections in combination with energy and momentum conservation, allows a complete reconstruction of the momentum sharing of the three fragments. First, using momentum conservation, the origin of each three-body dissociation event in the laboratory frame (x_0, y_0, z_0) can be determined; in the longitudinal direction (z) the result is explicitly

$$z_0 = t_s[m_{O^0} L_2/t_2 + m_{H^+} L_1(1/t_{1(1)} + 1/t_{1(2)}) - m_I v_I], \tag{9}$$

where the parameter t_s is defined as $1/t_s = m_O/t_2 + m_H/t_{1(1)} + m_H/t_{1(2)}$. The total kinetic-energy release in the three-body process is determined as

$$E_T = E_{H^+(1)} + E_{H^+(2)} + E_{O^0}, \tag{10}$$

where the individual fragment energies are obtained from Eq. (6), using the identified fragment masses. The resulting distribution of kinetic-energy release for the $O^0 + 2H^+$ channel is shown in Fig. 5(a).

We have evaluated the effect of the geometrical limitations of the detection system on the measured distribution of

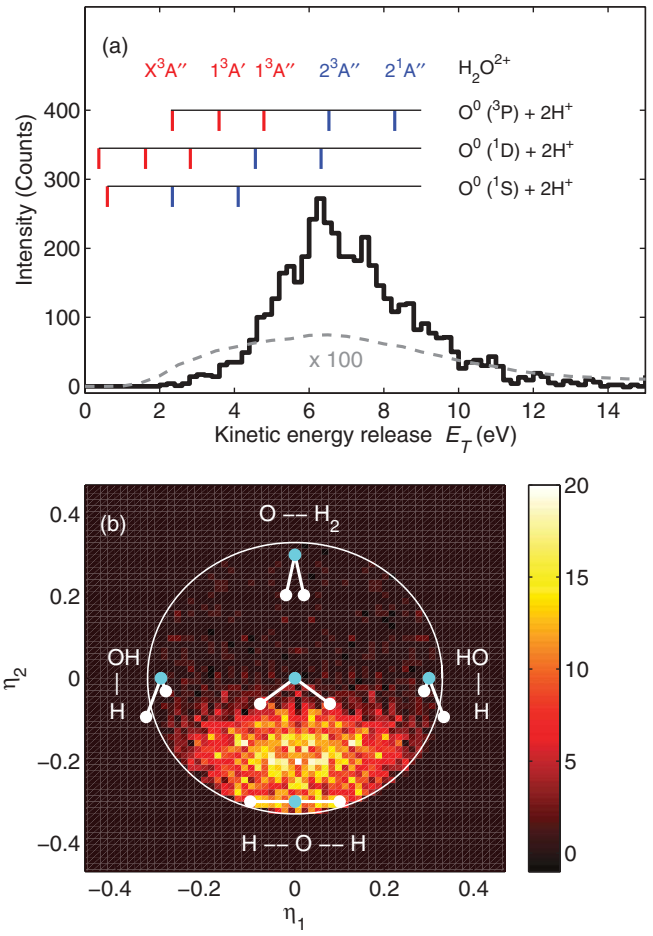

FIG. 5. (Color online) Photofragmentation H_2O^+ at 35.0 nm leading to three-body breakup into $O^0 + 2H^+$ studied by coincidence momentum imaging of the H^+ fragments detected with DET 1 and O^0 fragments detected with DET 2 (see Fig. 2). (a) Observed distribution (solid black line) of total kinetic-energy release E_T [Eq. (10)]. The gray dashed line shows the geometrical efficiency of the detection systems obtained from Monte Carlo simulations. The ladders above the experimental distribution show the expected kinetic-energy releases [44] (see Fig. 1) for vertical transitions from the vibronic ground state of H_2O^+ to five states of H_2O^{2+} followed by dissociation into three possible final states of $O^0 + 2H^+$. (b) Dalitz plot representing the momentum sharing in the fragmentation process [Eqs. (11) and (12)].

three-body kinetic-energy release E_T, using Monte Carlo simulations on samples of randomly oriented fragmenting H_2O^{2+} ions with uniformly distributed kinetic-energy releases in the range from 0 to 15 eV. From these results [dashed line in Fig. 5(a)], we find that the geometrical efficiency is relatively flat over the range of observed energies and conclude that it significantly affects the distributions only for $E_T \geqslant 9$ eV.

To gain insight into the angular correlation of the emerging photofragments in the three-body breakup process, we used Dalitz coordinates [54] (η_1, η_2) adapted to the case of a three-body system with two identical particles [55]:

$$\eta_1 = \sqrt{\frac{m_I}{3m_O}} \frac{E_{H^+(1)} - E_{H^+(2)}}{\sqrt{3} E_T} \tag{11}$$

and

$$\eta_2 = \frac{m_I}{3m_H}\frac{E_{O^0}}{E_T} - \frac{1}{3}. \quad (12)$$

These coordinates are linear combinations of the fragment energies, defined such that they are uniformly distributed in case of completely uncorrelated three-body breakup; that is, structures in the Dalitz plot signify preferred angular geometries in the dynamics of the dissociation. The particular mass-dependent factors used in Eqs. (11) and (12) result in a distribution confined by momentum conservation within a circle of radius 1/3 in an (η_1, η_2) diagram.

The Dalitz plot corresponding to the observed three-body dissociation of H_2O^{2+} is displayed in Fig. 5(b). A set of coordinates (η_1, η_2) corresponds to a particular momentum sharing of the three fragments, with the limiting situations indicated in the figure; here the plot displays a symmetry around $\eta_1 = 0$ since the two protons are identical particles. Evidently, the distribution shown in Fig. 5(b) reveals that the dissociation dynamics is dominated by processes where the two protons carry the most momentum away almost symmetrically from the central oxygen.

C. Two-body fragmentation dynamics: $H_2O^{2+} \rightarrow OH^+ + H^+$ and $O^+ + H_2^+$

As shown in Sec. III A (see Fig. 4) the fragments observed with DET 1 can be attributed to either three-body dissociation when observed in coincidence with a neutral oxygen or to two-body fragmentation processes leading to $OH^+ + H^+$ or $O^+ + H_2^+$. In fact, the characteristic distribution of kinetic-energy release for the two-body events can be obtained by subtraction of the known three-body distribution.

In the momentum images of Fig. 3(a), the lighter fragments H^+ and H_2^+ of a two-body decay occur as as half circles with a radius $\{[(m_I - m_F)/m_F]E_k/E_I\}$ related to the kinetic-energy release (E_k) of the active process. It should be noted that, through energy and momentum conservation, and disregarding the small effect of the interaction volume, the two-body fragmentation momentum is well represented by the observation of a single fragment; the coordinate of the interaction point (x_0, y_0, z_0) used in Eq. (1) is here determined from the center of the single particle distributions of these coordinates. Consequently, the bright circular shape corresponding to the light fragments of two-body decays appears in Fig. 3(a), while it is suppressed by the coincidence with a neutral heavy fragment [Fig. 3(c)], which in the present situation represents the contribution from three-body decay processes. Indeed, the absence of sharp structures in Fig. 3(c) shows that any contributions from nonionizing photodissociation, which could give rise to two-body decays involving a neutral fragment, as well as processes yielding $O^{2+} + H_2$, are absent.

Explicitly, the kinetic-energy release E_k in a two-body dissociation process is obtained from the momentum image as

$$E_k = \frac{\Delta p_F^2}{2\mu} = \left(\frac{\Delta p_F}{p_F}\right)^2 \frac{m_F}{m_I - m_F} E_I, \quad (13)$$

where μ is the reduced mass of the two-body system. From the momentum image shown in Fig. 3(a), it is evident that the geometrical limitations of the detection system must be taken into account to obtain a realistic distribution of kinetic energies for the active two-body processes; clearly, for $E_k(m_I - m_F)/m_F \geqslant 71.4$ eV, events with emission angles $60^\circ \leqslant \theta_F \leqslant 135^\circ$ are only partly registered. Thus, to obtain a representative distribution of kinetic energies for the active two-body processes we impose an angular selection of events outside the mentioned angular range for all energies. The resulting distribution of two-body dissociation energies is shown in Fig. 6. Provided that the angular distribution of photofragments is not a function of the kinetic-energy release, this distribution gives a correct representation of the two-body kinetic-energy release distribution despite the geometrical detection limitations

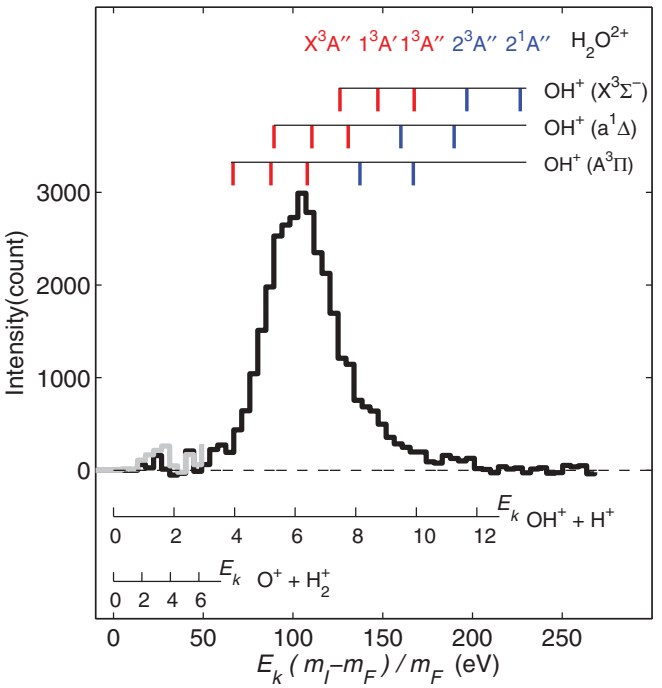

FIG. 6. (Color online) Photofragmentation of H_2O^+ at 35.0 nm leading to two-body breakup into $OH^+ + H^+$ and $O^+ + H_2^+$ at 35.0 nm studied by momentum imaging of the H^+ or H_2^+ fragment detected with DET 1 (Fig. 2). The black line shows the observed distribution of two-body kinetic-energy release with angular sections of events $\theta_F \leqslant 60^\circ$ or $\theta_F \geqslant 135^\circ$ [Eq. (5)]. The gray line shows the distribution including all fragment angles at low values of $E_k(m_I - m_F)/m_F$. The ladders above the experimental distribution show the expected kinetic-energy releases [44] (see Fig. 1) for vertical transitions from the vibronic ground state of H_2O^+ to five states of H_2O^{2+} followed by dissociation into three possible final states of $OH^+ + H^+$.

As demonstrated with the data in Fig. 4, by far most light particles impacting on DET 1 are protons originating from the breakup of the dication into $OH^+ + H^+$. The relevant kinetic energy release scale is indicated in Fig. 6. A smaller fraction of molecular hydrogen ions from the dissociation into $O^+ + H_2^+$ are also expected on DET 1, while most H_2^+ fragments pass through the central hole of DET 1. A second scale for E_k corresponding to this second channel also indicated in Fig. 6.

Considering the predicted energy releases for the two channels (see Fig. 1), we attribute the large peak centered at ~6 eV to originate from protons belonging to the $OH^+ + H^+$ channel.

A small structure is also observed at $E_k(m_I - m_F)/m_F \sim 25$. For events in this energy range, the angular selection of is not required and we also show the resulting distribution for all angles (gray line). We attribute the particles observed at these low values of $E_k(m_I - m_F)/m_F$ to be H_2^+ ions from the $O^+ + H_2^+$ channel.

IV. DISCUSSION

A. Fragmentation routes of H_2O^{2+}

The observed distributions of fragment kinetic-energy releases for three-body breakup of H_2O^{2+} [Fig. 5(a)] and its two-body breakup (Fig. 6) can be interpreted considering the vertical ionization energies calculated by Gervais *et al.* [44] from the $X\ ^2B_1$ ground state of H_2O^+, and the respective final-state energies. At this stage, we assume the precursor H_2O^+ ions to populate mainly their electronic ground state. The complete energy balance for the breakup process is

$$E_X = E_\gamma - E_e - E_c - E^i_{vJ} + E^f_{vJ}, \tag{14}$$

where E_X is the fragment kinetic-energy release, that is, E_T [Eq. (10)] for a three-body breakup and E_k [Eq. (13)] for a two-body breakup, E_γ the photon energy, E_e the energy of the emerging photoelectron, and E_c the electronic energy of the final dissociation channel relative to the ground-state energy of H_2O^+. Moreover, $E^i_{v,J}$ and $E^f_{v,J}$ represent the ro-vibrational energy in the initial (i) and final (f) states, respectively ($E^f_{vJ} = 0$ for a three-body breakup). The photoelectron energy (E_e) is not explicitly measured in the present experiment. Instead, we assume here that $E_\gamma - E_e$ is given by the vertical ionization energy of Gervais *et al.* [44]. With these assumptions, a range of possible assignments remains not only with respect to the final channel, but also with respect to the excitation state of H_2O^{2+} reached by the photoionization process.

Figure 5(a) shows the energetic information deduced this way from the level diagram of Fig. 1 in comparison to the observed three-body kinetic-energy release. Considering the calculated energies [44] the observed distribution is consistent with three-body fragmentation occurring mainly through the $2\ ^3A''$ and $2\ ^1A''$ states of H_2O^{2+} to the $O^0(^3P) + 2H^+$ limit, as well as through $2\ ^3A''$ to the $O^0(^1D) + 2H^+$ limit, while $O^0(^1S)$ final states are not found to be significant. Moreover, no significant three-body fragmentation appears to occur from the lower-lying H_2O^{2+} states, X^3A'' and $1\ ^3A'$, $1\ ^3A''$.

The extension of the distribution to high energies possibly indicates an important contribution from the singlet state $2^1A''$ of H_2O^{2+} into triplet $O^0(^3P) + 2H^+$ dissociation. Very large excursions to high initial energies would be required to explain the observed energy distribution by contributions from the lower-lying $2^3A''$ PES.

In comparison to the calculations of Gervais *et al.* [44] the experimental results thus confirm the three-body dissociation to occur through the $2^3A''$ and $2^1A''$ states of the di-cation, with probably a substantial contribution from $2^1A''$. A spectrum of kinetic-energy releases for three-body dissociation was not given in Ref. [44]; however, in comparison to the kinetic-energy release measured here (Fig. 5), such spectra could represent a sensitive test of theory. Thus, the shape of the kinetic-energy distribution depends on the shape of the involved PESs, as well as the branching ratios of the various channels. Moreover, the Dalitz plot shown in Fig. 5(b) reflects explicitly the angular correlation of the emerging fragments which could also support the development of theory for the dissociative PESs of the H_2O^{2+} dications.

In Fig. 6 the experimentally determined kinetic-energy release for two-body fragmentation ($OH^+ + H^+$) is compared to the calculated dissociation energies for several possible potential surfaces of the dication [44] and using the same assumptions as discussed above for the three-body channel.

The results are consistent with the prediction of Gervais *et al.* that only the lower three PESs of the dication lead to two-body dissociation. A more detailed assignment is not possible because of the close proximity among the available PESs. The study of Gervais *et al.* [44] focused on the system HDO^+ and showed only explicit spectra of kinetic-energy release for the $X\ ^3A''$ state of the dication. Moreover, no explicit report on the relative significances of the various dissociation routes was given. Thus, a detailed comparison between experiment and theory is not possible at this stage. However, the present results open the possibility of such a comparison for the case of H_2O^{2+}. Indeed, future experiments on the HDO^+ would also be very interesting with the present experimental system.

The distribution shown in Fig. 6 also reveals a small contribution at low values of $E_k(m_I - m_F)/m_F$, which we attribute to H_2^+ particles from the channel $O^+ + H_2^+$ as observed with DET 3 [Fig. 4(c)]. In order to increase the sensitivity to the $O^+ + H_2^+$ channel, the present experiment on H_2O^+ could be improved by using a higher initial beam energy or a bias on the interaction zone (V_c), which would allow also the H^+ and H_2^+ fragments to reach DET 3.

By using the monocations as a precursor in this experiment, we study the PESs of H_2O^{2+} at the nuclear geometry of H_2O^+. For the ground-state of H_2O^+, as in the present case, this corresponds to nonbound geometries of the water dication. On the other hand, while the water dication itself has never been observed experimentally as a separate species, theoretical investigations suggest that the ground and first excited states of H_2O^{2+} have local minima at linear geometry ($D_{\infty h}$) [43]. Since the first excited state of the H_2O^+ has such a linear geometry, the technique used in the present experiment opens the possibility to study the quasibound potentials of H_2O^{2+} by preparing the precursor H_2O^+ ions in their first excited electronic state, following the previous proposal by Gervais *et al.* [44].

In the present experiment being our first study on xuv-induced photofragmentation of H_2O^+, no particular effort was made to prepare the ions in a well-defined initial state. The delay for the H_2O^+ ions to reach the interaction region following their production in the ion source amounts to $\sim 30\ \mu s$ in the present experiment. From previous experiments it can be estimated that a possible electronic excitation from the $\tilde{A}\ ^2A_1$ and the $\tilde{B}\ ^2B_2$ states would relax on a time scale of tens of μs [49,50], while a theoretical calculation [51] predicted vibrational excitation within the electronic ground state ($\tilde{X}\ ^2B_1$) to relax on a time scale of ms. It is thus likely that a fraction of the ions in this experiment reached the interaction region with vibrational excitation, while residing mainly in the ground state of H_2O^+. In a separate experiment [52] we have investigated the presence of electronically excited states

in the beam and found it to constitute ∼0.1% of the total beam. The TIFF experimental setup in fact also includes an electrostatic ion trap that in future experiments could allow for cooling of the precursor ions before irradiation by FLASH, as demonstrated in a recent experiment on HeH^+ [53].

Moreover, the possibility to make coincidence photofragment-photoelectron spectroscopy has recently been demonstrated with the TIFF apparatus [48], which could open for energically complete measurements according to Eq. (14). Such measurements would, in particular, allow for the vibrational excitation of the OH^+ fragment to be analyzed.

B. H_2O^{2+} formation by ionizing radiation

Aside of analyzing the dissociation properties of the dicationic states, the present experiment also allows conclusions about the H_2O^{2+} states reached by *direct* photoionization of the monocation.

The products of H_2O^{2+} fragmentation after *double* photoionization of neutral H_2O have been studied both in the soft x-ray [29–35] and uv-xuv [36–39] regimes. In the x-ray regime, inner-shell excitation and ionization dominates the photoaborption of neutral H_2O, leading to a multitude of fragmentation routes [30] that cannot easily be compared to the present results. In the xuv regime, double photoionization of neutral H_2O has been observed to lead to major fragmentation channels of $OH^+ + H^+$ and $O^+ + H^+ + H^0$ [36,37]; for the HDO^+ system, also a significant fraction of $O^0 + D^+ + H^+$ was reported [36], while a channel with O^0 was not observable for H_2O and D_2O with the technique used.

The fragmentation of H_2O^{2+} formed in collisions between neutral H_2O and ionizing radiation in the form of energetic *electrons* has also been addressed in a number of studies [26–28]. Tan *et al.* [26] reported the principal fragmentation channels of dications formed in electron-collisions with neutral H_2O to be $OH^+ + H^+$ and $O^+ + H^+ + H^0$, with a marginal contribution from from $O^+ + H_2{}^+$. More recent crossed-beams experiments [27,28], have determined almost equal intensity for $OH^+ + H^+$ and $O^+ + H^+ + H^0$ and much lower intensity for $O^{2+} + 2H^0$ (2%).

The main fragmentation channels of water dications formed by double photoionization [36,37] and electron-impact double [26–28] ionization of neutral water are thus very similar to each other. Indeed, in both cases double ionization has been interpreted to be dominated by a two-step mechanism with initial ionization of an electron from the $2a_1$ (inner valence) orbital of water followed by dissociative autoionization.

The results presented here from direct photoionization of H_2O^+ to form H_2O^{2+} are qualitatively different from those of uv-xuv photoabsorption [36–39] and electron-impact double ionization [26–28] of neutral water. We observe as a dominating channel $O^0 + 2H^+$ and do not observe significant contributions of $O^+ + H^+ + H^0$. This difference supports the two-step mechanism driven by autoionization from a $2a_1$ vacancy of H_2O as suggested in Ref. [27,28], resonant excitation of the $2a_1$ orbital not being possible in the present experiment. Interestingly, the fragmentation experiments on neutral water implying xuv photoabsorption [36,37] and electron neutral collisions [26–28] for experimental reasons inherently could not observe the three-body channel $O^0 + 2H^+$. Our finding of this channel as a major fragmentation route of H_2O^{2+}, as produced by photoabsorption as well as its observation for the HDO system [36], rise the question of the possible importance of this channel also in the photon- and electron-double ionization of neutral water.

Fragmentation of the water dication has also been studied in experiments employing ionizing radiation in the form of fast, often highly charged *ions* impacting on neutral water molecules [19–24]. Such collisions imply a strong interaction with the target that can lead to fast stripping of valence electrons [23], hence producing dications in the geometry of the neutral precursor directly, that is, without the stepwise ionization following photon or electron impact on H_2O. For such experiments, in fact, results more similar to the present experimental outcome are expected where single-ionization from different orbitals of the monocation also directly accesses the PESs of the dication.

Indeed, in a recent experiment detecting ionic dissociation fragments, Legendre *et al.* [23] reported on the fragmentation of HDO^{2+} produced by Ni^{25+} at 11.7 MeV/u impacting on neutral water molecules, and observed fragmentation into $OH^+ + D^+$, $OD^+ + H^+$, and $O^0 + H^+ + D^+$ (albeit without registering the O^0 fragment), similar to the channels observed in the present experiment. The $O^+ + H_2{}^+$ or $O^+ + HH^+$ channels were not reported in Ref. [23]. For HDO^{2+} produced by impact of highly charged ions, Legendre *et al.* [23] found a ratio of two-body ($OH^+ + H^+$ or $OD^+ + D^+$) and three-body ($O^0 + H^+ + D^+$) dissociation of ∼0.5, in reasonable agreement with the ratio of >0.7 [Eq. (8)] determined in the present experiment for H_2O^{2+}. In a further comparison, the kinetic-energy release found by Legendre *et al.* [23] for two-body dissociation compares well with present results, while their reported three-body kinetic-energy release peaks at ∼9 eV and is thus higher than the three-body kinetic-energy release found in the present work. The difference in the fragment branching ratio and the three-body kinetic-energy release most likely shows evidence for different initial states of dicationic H_2O^{2+} formed in the two ionization processes: Highly charged ions can be assumed to produce all possible valence stripped molecules, while photoionization will produce a more limited number of states reached by ionization of single electrons from H_2O^+.

V. CONCLUSION

With the present crossed ion-photon beam experiment performed with an intense free electron laser [17], we have taken a first step in characterizing the photolysis of the water cation H_2O^+ in the xuv regime.

In particular, we interpret our results assuming that the photofragmentation of H_2O^+ proceeds the formation of dications, H_2O^{2+}, that dissociate mainly into three product channels, namely $O^0 + 2H^+$, $OH^+ + H^+$, and $O^+ + H_2{}^+$, and we determine the ratios $\sigma_{OH^+ + H^+}/\sigma_{O^+ + H_2{}^+} = 4.2 \pm 0.3$ and $\sigma_{OH^+ + H^+}/\sigma_{O^0 + 2H^+} > 0.7$.

By comparing of the measured kinetic-energy releases for three-body breakup ($O^0 + 2H^+$) and two-body breakup into $OH^+ + H^+$ to recent calculations [44], Our observations agree with the predicted tendency that the $2^3A''$ and $2^1A''$ states

of H_2O^{2+} mainly dissociate into $O^0 + 2H^+$, while the states X^3A'', $1^3A'$, and $1^1A''$ dominantly dissociate into $OH^+ + H^+$. Finally, the present experiments reveal that the fragmentation into $O^0 + 2H^+$ is characterized by a dynamics where the two emerging protons dissociate in a near-linear geometry and carry the major part of the released momentum.

ACKNOWLEDGMENTS

This work has been supported by the Max-Planck Advanced Study Group at CFEL Hamburg and the Max-Planck Society. H.B.P. acknowledges support from the Lundbeck foundation. We greatly thank the scientific and technical staff [18] at FLASH for their invaluable support.

[1] G. Herzberg, Ann. Geophys. **36**, 605 (1980).
[2] P. Wehinger, S. Wyckoff, and G. H. Herbig, G. Herzberg, and H. Lew, Astrophys. J. **190**, L43 (1974).
[3] P. Wehinger and S. Wyckoff, Astrophys. J. **192**, L41 (1974).
[4] A. H. Delsemme and M. R. Combi, Astrophys. J. **209**, L153 (1976).
[5] W.-H. Ip, U. Fink, and J. R. Johnson, Astrophys. J. **293**, 609 (1985).
[6] N. Meyer-Vernet, M. A. Strauss, J. L. Steinberg, H. Spinrad, and P. J. McCarthy, Astron. J **93**, 474 (1987).
[7] M. A. Disanti, U. Fink, and A. B. Schultz, Icarus **86**, 152 (1990).
[8] D. A. Neufeld *et al.*, Astron. Astrophys. **521**, L10 (2010).
[9] H. Gupta *et al.*, Astron. Astrophys. **521**, L47 (2010).
[10] V. Ossendorf *et al.*, Astron. Astrophys. **518**, L111 (2010).
[11] M. Gerin *et al.*, Astron. Astrophys. **518**, L110 (2010).
[12] E. F. van Diskoeck and J. H. Black, Astrophys. J. Ser. **62**, 109 (1986).
[13] D. Smith, Chem. Rev. **92**, 1473 (1992).
[14] D. J. Hollenbach and A. G. G. M. Tielens, Annu. Rev. Astron. Astrophys **35**, 179 (1997).
[15] D. J. Hollenbach, M. J. Kaufman, E. A. Bergin, and G. J. Melnick, Astrophys. J. **690**, 1497 (2009).
[16] P. R. Maloney, D. J. Hollenbach, and A. G. G. M. Tielens, Astrophys. J. **466**, 561 (1996).
[17] W. Ackermann *et al.*, Nat. Photon. **1**, 336 (2007).
[18] K. Tiedtke *et al.*, New J. Phys. **11**, 023029 (2009).
[19] J. C. Severs, F. M. Harris, S. R. Andrews, and D. E. Parry, Chem. Phys. **175**, 467 (1993).
[20] G. H. Olivera, C. Caraby, P. Jardin, A. Cassimi, L. Adoui, and B. Gervais, Phys. Med. Biol. **43**, 2347 (1998).
[21] B. Siegmann, U. Werner, H. O. Lutz, and R. Mann, J. Phys. B **34**, L587 (2001).
[22] F. Alvarado, R. Hoekstra, and T. Schlathölter, J. Phys. B **38**, 4085 (2005).
[23] S. Legendre, E. Giglio, M. Tarisien, A. Cassimi, B. Gervais, and L. Adoui, J. Phys. B **38**, L233 (2005).
[24] A. M. Sayler, M. Leonard, K. D. Carnes, R. Cabrera-Trujilo, B. D. Esry, and I. Ben-Itzhak, J. Phys. B **39**, 1701 (2006).
[25] Moddeman *et al.*, J. Chem. Phys. **55**, 2317 (1971).
[26] K. H. Tan *et al.*, Chem. Phys. **29**, 299 (1978).
[27] S. W. J. Scully, J. A. Wyer, V. Senthil, M. B. Shah, and E. C. Montenegro, Phys. Rev. A **73**, 040701(R) (2006).
[28] E. C. Montenegro, S. W. J. Scully, J. A. Wyer, V. Senthil, and M. B. Shah, J. Electron Spectrosc. Relat. Phenom. **155**, 81 (2007).
[29] H. Siegbahn, L. Asplund, and P. Kelfve, Chem. Phys. Lett. **35**, 330 (1975).
[30] M. N. Piancastelli, A. Hempelmann, F. Heiser, O. Gessner, A. Rüdel, and U. Becker, Phys. Rev. A **59**, 300 (1999).
[31] M. N. Piancastelli, R. Sankari, S. Sorensen, A. De Fanis, H. Yoshida, M. Kitajima, H. Tanaka, and K. Ueda, Phys. Rev. A **71**, 010703(R) (2005).
[32] A. Hiraya *et al.*, Phys. Rev. A **63**, 042705 (2001).
[33] W. C. Stolte, M. M. Sant'Anna, G. Öhrwall, I. Dominguez-Lopez, M. N. Piancastelli, and D. W. Lindle, Phys. Rev. A. **68**, 022701 (2003).
[34] K. Ueda, J. Phys. B **36**, R1 (2003).
[35] A. Kiviäki, M. Coreno, R. Richter, J. A. Ruis, E. M. Garcia, M. de Simone, V. Freyer, G. Vall-Illosera, and K. C. Prince, J. Phys. B **39**, 1101 (2006).
[36] P. J. Richardson, J. H. D. Eland, P. G. Fournier, and D. L. Cooper, J. Chem. Phys. **84**, 3189 (1986).
[37] D. Winkoun, D. Dujardin, L. Hellner, and M. J. Besnard, J. Phys. B **21**, 1385 (1988).
[38] J. D. Eland, Chem. Phys. **323**, 391 (2006).
[39] S. Y. Truong, A. J. Yencha, A. M. Juarez, S. J. Cavanagh, P. Bolognesi, and G. C. King, Chem. Phys. Lett. **474**, 41 (2009).
[40] H. Ågren, S. Svensson, and U. I. Wahlgren, Chem. Phys. Lett. **35**, 336 (1975).
[41] W. Koch, N. Heinrich, H. Schwartz, F. Maquin, D. Stahl *et al.*, Int. J. Mol. Spectrom. Ion Processes **67**, 305 (1985).
[42] P. R. Bunker *et al.*, J. Mol. Spectrosc. **198**, 371 (1999).
[43] T. J. van Huis *et al.*, J. Chem. Phys **110**, 11856 (1999).
[44] B. Gervais, E. Giglio, L. Adoui, A. Cassimi, D. Duflot, and M. E. Galassi, J. Chem. Phys. **131**, 024302 (2009).
[45] A. G. Sage, T. A. A. Oliver, R. N. Dixon, and M. N. R. Ashfold, Mol. Phys. **108**, 945 (2010).
[46] H. B. Pedersen *et al.*, Phys. Rev. A **80**, 012707 (2009).
[47] M. Martins *et al.*, Rev. Sci. Instrum. **77**, 115108 (2006).
[48] L. S. Harbo, A. Becker, S. Dziarzhytski, C. Domesle, N. Guerassimova, A. Wolf, and H. B. Pedersen, Phys. Rev. A **86**, 023409 (2012).
[49] G. R. Möhlmann, K. K. Bhutani, F. J. de Heer, and Tsurubuchi, Chem. Phys. **31**, 273 (1978).
[50] K. Norwood and C. Y. Ng, J. Chem. Phys. **95**, 8029 (1991).
[51] B. Weis, C. Carter, P. Rosmus, H.-J. Werner, and P. J. Knowles, J. Chem. Phys. **91**, 2818 (1989).
[52] L. S. Harbo, A. Becker, S. Dziarzhytski, C. Domesle, N. Guerassimova, A. Wolf, and H. B. Pedersen (unpublished).
[53] H. B. Pedersen, L. Lammich, C. Domesle, B. Jordon-Thaden, O. Heber, J. Ullrich, R. Treusch, N. Guerassimova, and A. Wolf, Phys. Rev. A **82**, 023415 (2010).
[54] R. H. Dalitz, Phys. Rev. **94**, 1046 (1954).
[55] D. Strasser, L. Lammich, H. Kreckel, M. Lange, S. Krohn, D. Schwalm, A. Wolf, and D. Zajfman, Phys. Rev. A **69**, 064702 (2004).